

Single ferroelectric and chiral magnetic domain of single-crystalline BiFeO₃ in an electric field

Seongsu Lee,¹ Taekjib Choi,¹ W. Ratcliff II,² R. Erwin,² S-W. Cheong,¹ and V. Kiryukhin¹

¹*Department of Physics and Astronomy and Rutgers Center for Equivalent Materials, Rutgers University, Piscataway, New Jersey 08854, USA*

²*NIST Center for Neutron Research, NIST, Gaithersburg, Maryland 20899, USA*

(Received 12 June 2008; revised manuscript received 11 August 2008; published 11 September 2008)

We report on polarized neutron-scattering and piezoresponse force microscopy studies of millimeter-sized single crystals of multiferroic BiFeO₃. The crystals, grown below the Curie temperature, consist of a single ferroelectric domain. Two unique electric polarization directions, as well as the populations of equivalent spiral magnetic domains, can be switched reversibly by an electric field. A ferroelectric monodomain with a single-*q* single-helicity spin spiral can be obtained. This level of control, so far unachievable in thin films, makes single-crystal BiFeO₃ a promising object for multiferroics research.

DOI: 10.1103/PhysRevB.78.100101

PACS number(s): 77.80.Dj, 77.80.Fm, 75.80.+q

Understanding and controlling of domain structure are crucial for applications of magnetic and ferroelectric materials, as well as for studies of their intrinsic properties. Coercivity of permanent magnets, switching of memory devices, and many other functional properties are defined by domain physics. Ferroelectricity and magnetism coexist in multiferroics.¹ These materials have attracted significant attention recently because of an intriguing possibility of control of their magnetic properties with an electric field and vice versa,²⁻⁴ leading to the discovery of new physical phenomena and fabrication of novel devices.⁵ So far, little research has been done on the domain structure of multiferroics. Among a few notable exceptions⁶ is BiFeO₃ (BFO), but mostly in its thin-film form, since suitable single crystals were unavailable. BFO is arguably the most extensively studied multiferroic due to its large polarization at room temperature.⁴ Importantly, this is the only multiferroic exhibiting large effects of an electric field on the magnetic structure, as first demonstrated in thin films,² and subsequently in single crystals.^{7,8} Unfortunately, BFO thin films exhibit poor crystallinity and are influenced by substrate strain,^{2,5} impeding studies of BFO's intrinsic properties, and complicating device fabrication. Herein, we report on studies of single-crystal BFO in which an unprecedented level of control of domains and their electric and magnetic properties can be achieved.

BFO is ferroelectric for $T < T_C \approx 850$ °C. It exhibits the rhombohedral $R3c$ structure with a perovskite pseudocubic unit cell ($a \approx 3.96$ Å, $\alpha \approx 89.4^\circ$) elongated along the (111) direction, which coincides with the electric polarization vector \mathbf{P} .⁹ For $T < T_N \approx 370$ °C, Fe spins exhibit the *G*-type antiferromagnetic order.¹⁰ In single crystals, there is an additional long-range ($\lambda \approx 620$ Å) magnetic modulation with the wave vector $\tau_1 = (\delta, 0, -\delta)$ believed to be cycloidal with antiparallel spins slowly rotating in the plane containing \mathbf{P} and τ .⁹ Wave vectors $\tau_2 = (\delta, -\delta, 0)$ and $\tau_3 = (0, -\delta, \delta)$ are equivalent by symmetry, giving three propagation directions each perpendicular to \mathbf{P} . The spins are rigidly coupled to the crystal lattice and rotation of \mathbf{P} between the different cubic body diagonals by an electric field results in the rotation of the magnetic structure.^{2,7,8} This effect was recently used to demonstrate the local control of magnetization by an electric field.⁵

BFO exhibits four structural variants (ferroelastic domains) based on the four different cubic body diagonals and eight possible directions of \mathbf{P} (ferroelectric domains) shown in Fig. 1(a). To produce any realistic device and to study the intrinsic properties, single-domain samples are needed. However, despite significant efforts, the best available BFO thin films always consist of micrometer-sized ferroelastic domains.^{2,5} Films with suitable electrical characteristics are of the (001) type and therefore poling (electric field applied along the cubic direction) is inappropriate for getting rid of the ferroelastic domains. In single crystals, poling in the (111) direction might be possible, but the situation is complicated by the presence of the equivalent magnetic domains in a single ferroelectric domain, as shown in Fig. 1(b). In this work, we report on preparation of millimeter-sized single crystals with a single ferroelectric and single- τ magnetic domain, see Fig. 1(c). The magnetic state is chiral as in a single-helicity spiral. The electric and magnetic states can be reversibly controlled by an electric field, which switches the electric polarization between the two unique states shown in Fig. 1(d), and also controls the equivalent magnetic domains. These results open different opportunities for studies of BFO and for BFO-based device fabrication.

Single crystals of BFO were grown using a

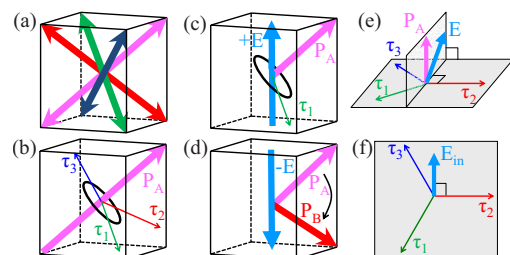


FIG. 1. (Color online) (a) Possible electric polarization directions in the pseudocubic cell of BiFeO₃. (b) Equivalent magnetic spirals in a single ferroelectric domain. (c) A single ferroelectric/magnetic domain state. (d) Switching of the ferroelectric domains in an applied field. (e) and (f) show the orientation of E with respect to τ_1 , τ_2 , and τ_3 and its projection E_{in} on the plane containing these vectors. For simplicity, only one antiferromagnetic sublattice in the spirals is shown and the modulation wavelength is decreased.

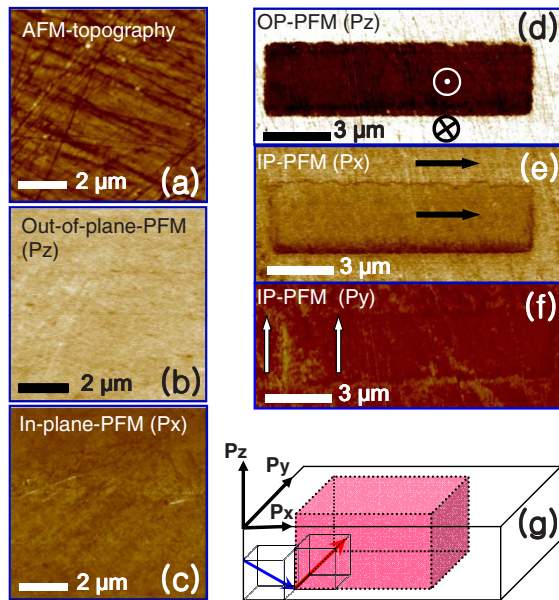


FIG. 2. (Color online) Representative (a) atomic force microscopy (AFM) and [(b) and (c)] PFM images of the (001) surface. (d) Out-of-plane and [(e) and (f)] in-plane PFM images of a ferroelectric domain created by a biased PFM tip. Arrows indicate the polarization direction probed in each image. The polarization vectors in the ferroelectric domains are shown schematically in (g).

$\text{Bi}_2\text{O}_3/\text{Fe}_2\text{O}_3/\text{B}_2\text{O}_3$ flux by slow cooling from 870 °C to 620 °C. Crystals with $\sim\text{mm}^2$ -area natural faces normal to the cubic directions were obtained. Piezoresponse force microscopy (PFM) was performed with a commercial scanning probe microscope. P_x , P_y , and P_z components of \mathbf{P} were measured, with P_z normal to the sample surface, and the axes coinciding with the pseudocubic directions. For electric domain switching, a 40 V bias (bottom electrode) was applied to a 20- μm -thick sample, with the PFM tip grounded. Neutron experiments were done at $T=50$ K on BT9 and BT7 (polarized measurements) triple-axis spectrometers at NIST Center for Neutron Research at an energy of 14.7 meV with collimations 40–10-s-40–80 (BT9) and 25–10-s-50 (BT7).

The collimations were set such that their further tightening would result either in no significant resolution improvement or in unacceptable signal losses, ensuring the best possible resolution compatible with our signal level. Two parallel gold contacts were evaporated on the largest faces of a $3 \times 2 \times 1$ mm³ sample for an electric field E to be applied in the (001) direction.

Different ferroelastic domains can be easily detected using our neutron-scattering setup.⁷ The only Bragg peaks found in our samples were due to a single domain, even though a careful search for other domains was done. Considering the experimental accuracy, we conclude that more than 95% of each studied sample consists of a single ferroelastic domain. Multiple PFM measurements show the same P_x , P_y , and P_z across the surface in the majority of as-prepared samples. Typical images are shown in Figs. 2(a)–2(c). Thus, the samples consist of a single ferroelectric domain. Local electric polarization can be switched reversibly by an application of E normal to the (001) surface by the PFM tip. Figures 2(d)–2(f) show that while P_z changes its direction in the region of bias application, P_x and P_y remain unchanged in the process. Thus, \mathbf{P} rotates by 71° as shown in Figs. 1(d) and 2(g), the rotation direction is unique, and no 109° or 180° domains are created. This observation is in agreement with theoretical calculations showing that the elastic energy losses are minimal for the 71° domain boundaries.¹¹

We now turn to the magnetic structure of the equivalent magnetic domains τ_1 , τ_2 , and τ_3 in the ferroelectric domain \mathbf{P}_A of Fig. 1(b). Figure 3 shows unpolarized neutron-scattering pattern near the $(1/2, -1/2, 1/2) \pm \tau$ magnetic peak in the $(h, -h, l)$ plane, with projections of all the three magnetic wave vectors marked. Only the \mathbf{P}_A -domain signal is detected in this geometry, even when the second ferroelectric domain (\mathbf{P}_B in Fig. 1) starts appearing for $E < 0$ (see Ref. 7 for the discussion of the \mathbf{P}_B -domain magnetism). For $E=0$, two magnetic domains with wave-vectors τ_1 and τ_2 are present. Application of E at an acute angle of 55° to \mathbf{P} , as shown in Fig. 1(c), suppresses domain τ_2 . For $E=1.3$ MV/m, only domain τ_1 is observed within the accuracy of our measurement ($\sim 10\%$ of the domain population), see Fig. 3(b). This figure shows that a fit to two Gaussian

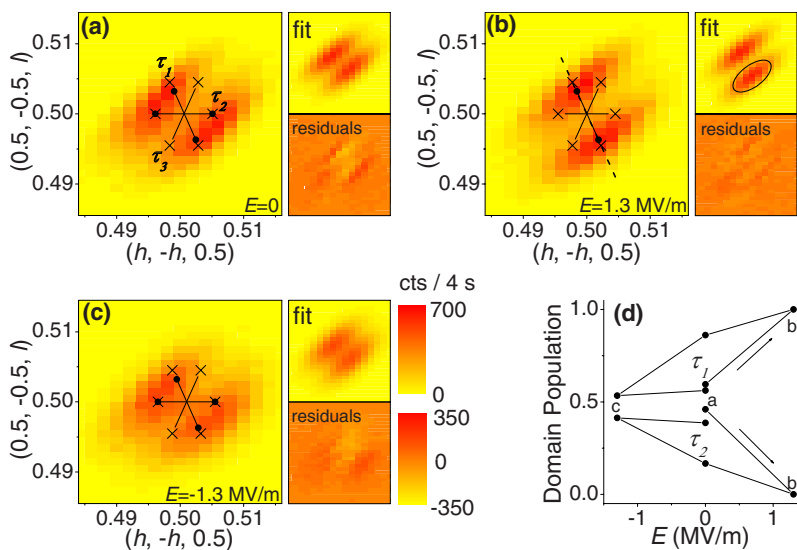


FIG. 3. (Color online) Magnetic peaks near the $(1/2, -1/2, 1/2)$ position in the $(h, -h, l)$ plane for (a) $E=0$ in the as-prepared sample, for (b) $E=1.3$ MV/m, and for (c) $E=-1.3$ MV/m. The ellipse in (b) shows the calculated instrumental resolution. Crosses indicate projections of the τ_1 , τ_2 , and τ_3 peaks on the scattering plane. Circles show the positions of the peaks used in the fits described in the text. The fits and the residuals are shown to the right of the main panels. Populations of the magnetic domains τ_1 and τ_2 determined in these fits are shown in (d) as functions of E .

peaks at $\pm\tau_1$, with the widths and orientation closely matching the calculated resolution, reproduces the data very well. Note that for the out-of-scattering-plane vector τ_1 , the peak positions differ slightly from their projections on the scattering plane due to resolution effects. Thus, the entire crystal consists of a single- τ magnetic domain, as shown schematically in Fig. 1(c). Sufficiently large negative E produces the opposite effect, enriching domain τ_2 at the expense of τ_1 , see Fig. 3(c). This effect is probably driven by the uniaxial piezoelectric strain, which is linearly coupled to E . Figures 1(e) and 1(f) show that the field projection on the plane containing τ_1 , τ_2 , and τ_3 is normal to τ_2 and, therefore, the induced strain lifts the symmetry making the domains equivalent in zero field. Note that τ_2 is the only common magnetic wave vector for \mathbf{P}_A and \mathbf{P}_B domains, which may play a role in its stabilization for $E < 0$. The absence of domain τ_3 is probably related to the postgrowth residual strain. To characterize the magnetic domain populations, the neutron data were modeled by four Gaussian peaks of the same shape (measured at $E = 1.3$ MV/m), see Figs. 3(a)–3(c). For τ_1 , the peaks were located in the experimental positions found at $E = 1.3$ MV/m. For the in-plane τ_2 , the peaks were located in the theoretical positions. As functions of E , the domain populations form reproducible hysteresis loops, showing electric-field control of the magnetic domains, see Fig. 3(d). While higher-resolution measurements are needed to reveal the details of these loops, our data strongly suggest that any specific magnetic domain can be stabilized by application of the appropriate uniaxial stress, and that complete control of the magnetic state can thus be achieved in BFO.

Cycloidal magnetic state is believed to be realized in BFO,⁹ but alternatives were also proposed.¹² While recent single-crystal neutron studies support the cycloid,⁸ noncollinear states are difficult to analyze and further work is needed to establish the magnetic state unambiguously. Various magnetic interactions can produce the cycloid. Common cases include competing nearest- and next-nearest-neighbor exchange and antisymmetric Dzyaloshinsky-Moria (DM) and magnetoelectric¹³ interactions.¹ In the (1–10) FeO chains in ferroelectric BFO, all the exchange-mediating oxygens are shifted from symmetric positions with respect to Fe in the same direction along \mathbf{P} .⁹ For such shifts, the magnetoelectric interaction is proportional to $P(m_y L_x - m_x L_y)$, where m is the unit magnetization, L is the antiferromagnetic vector, and the xy plane is defined as normal to the direction of \mathbf{P} .¹³ It is of the same form as the DM interaction and should produce a weakly ferromagnetic spiral^{13,14} with rotation direction (helicity) uniquely defined in the rotation plane by $\mathbf{P} \sim \mathbf{e} \times \boldsymbol{\tau}$, where \mathbf{e} is the spin rotation axis,¹ see insets in Fig. 4. Nonzero \mathbf{P} is essential for the chiral state, i.e., the spiral is induced by \mathbf{P} , which appears at T much higher than T_N . (Note that this is different from magnetically driven ferroelectrics such as RMnO_3 in which the situation is reversed and \mathbf{P} is induced by the inverse DM interaction in a magnetic spiral.¹) We used polarized neutron scattering to characterize the helicity of the spiral. Scans were taken in both of the spin-flip channels, denoted as (+–) and (–+), with neutrons polarized parallel to the scattering vector \mathbf{Q} . Scattering cross section¹⁵ is proportional to $\langle S_{\perp Y} S_{\perp Y}^* \rangle + \langle S_{\perp Z} S_{\perp Z}^* \rangle \pm i \langle \langle S_{\perp Y} S_{\perp Z}^* \rangle - \langle S_{\perp Z} S_{\perp Y}^* \rangle \rangle$, where $\langle AB^* \rangle \equiv \sum \exp(i\mathbf{Q}\mathbf{r}_j) A(\mathbf{0}) B^*(\mathbf{r}_j)$,

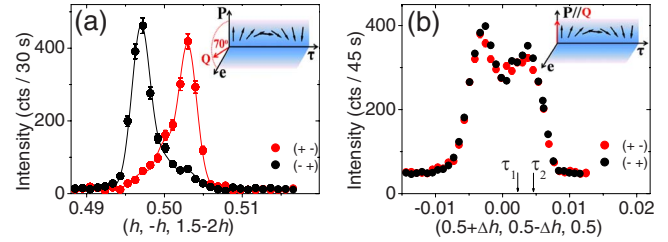


FIG. 4. (Color online) Polarized neutron scans in the (+–) and (–+) spin-flip channels. (a) $(h, -h, 1.5-2h)$ scan through domain τ_1 near the $(1/2, -1/2, 1/2)$ position in the $(h, -h, l)$ plane. The direction of this scan is shown in Fig. 3(b) with dashed line. Error bars are from counting statistics. (b) $(0.5+\Delta h, 0.5-\Delta h, 0.5)$ scan through domains τ_1 and τ_2 near the $(1/2, 1/2, 1/2)$ position in the $(h, 2l-h, l)$ plane. Arrows show the positions of the peaks due to these domains. Insets show the orientation of the scattering vector \mathbf{Q} with respect to the plane of the magnetic spiral, as well as vectors \mathbf{e} , \mathbf{P} , and $\boldsymbol{\tau}$.

$\mathbf{S}_{\perp} = \mathbf{Q} \times (\mathbf{S} \times \mathbf{Q})$, \mathbf{S} is the spin at the position \mathbf{r}_j , and the coordinate axes X and Z run along \mathbf{Q} and normal to the scattering plane, respectively. It depends on the helicity of the spiral and on the angle between \mathbf{e} and \mathbf{Q} : The difference between the channels is maximal for $\mathbf{e} \parallel \mathbf{Q}$ and is absent for $\mathbf{e} \perp \mathbf{Q}$. Figure 4(a) shows scans through the $(1/2, -1/2, 1/2) \pm \tau_1$ peaks in the $(h, -h, l)$ plane in the single-domain state of Fig. 3(b). The direction of this scan is shown in Fig. 3(b) with a dashed line. In this geometry, the intensity ratio of the $+\tau_1$ and $-\tau_1$ peaks, calculated for the spiral rotating in the plane of \mathbf{P} and τ_1 , is ~ 8 . The data of Fig. 4(a) fit well to the sum of these peaks with the intensity ratio of 9 and a weak central peak, possibly coming from $\lambda/2$ contamination. Note that for any nonchiral structure, such as a spin-density wave, or for a sample equally populated with spirals of both helicities, both the τ_1 peaks should be of the same intensity. Figure 4(b) shows scans through a different magnetic peak, $(1/2, 1/2, 1/2) \pm \tau$, in the $(h, 2l-h, l)$ scattering plane in the two-domain state of Fig. 3(a). As discussed in Ref. 7, the τ_1 and τ_2 domains produce peaks in the $\pm\delta/2$ and $\pm\delta$ positions, respectively, in these scans, giving rise to the broad peaks of Fig. 4(b). In this geometry, \mathbf{e} is normal to \mathbf{Q} and no difference between the (+–) and (–+) channels is observed as expected. Thus, our data provide strong evidence for the spiral model discussed in the literature.⁹ Moreover, we show that magnetic domains are fully chiral (contain a single-helicity spiral for a given τ) as expected on symmetry grounds.

Spontaneous formation of large single crystals containing a single ferroelastic, ferroelectric, and (upon application of an electric field) single- τ chiral magnetic domain—while seemingly surprising—was achieved by design. B_2O_3 was added to the flux to reduce the liquidus temperature down to ~ 620 °C, thus allowing the crystals to grow below T_C in the polar state.¹⁶ Effectively, the system behaves as a pyroelectric and formation of a unipolar ferroelectric domain is favored. While the growth temperature was not measured directly, we found that annealing the crystals at T_C produces ferroelastic domains, strongly supporting this mechanism. The origin of the chiral magnetic state lies in the symmetry

of the system, which fixes the helicity of the spiral once \mathbf{P} and τ are chosen, as observed in our experiments.

The above data demonstrate that high level of control of electric and magnetic properties can be achieved in single-crystal BFO. The samples contain a single ferroelectric domain, reversible ferroelectric switching occurs between only two well-defined polarization states, and a single- τ magnetic chiral domain can be stabilized by piezoelectric strain. Note that 50- μm -thick single-domain crystals were reported in Refs. 8 and 16, but no reversible control of \mathbf{P} and no control of the equivalent magnetic domains were achieved, and the chirality was not measured. Also, as shown previously, the magnetic structure rotates together with \mathbf{P} when an electric field is applied.^{7,8} Such level of control is currently unachievable in thin films, which consist of a patchwork of ferroelastic microdomains, with domain-dependent properties in an applied field.^{2,5} Single-crystal BFO is therefore suitable for studies of intrinsic properties of this multiferroic, as well as for fabrication of devices with precisely controlled properties. Our results may also help identify prospective approaches for the growth of uniform thin films. Finally, BFO provides an intriguing example of successful “chiral resolution,”¹⁷ in which a large single crystal is prepared in a chiral magnetic state. This result reveals the symmetries involved in the coupling between the magnetic and electric

order parameters in BFO. Chirality and the inversion symmetry are strongly coupled in BFO as they are in many other multiferroics, such as TbMnO_3 , in which the chirality is also coupled to an electric field.¹⁸ Functional properties of these materials are defined by the underlying symmetry, and understanding the symmetry is essential for control and application of these properties.

In summary, we report on preparation of millimeter-sized single crystals of BFO, which grow below the Curie temperature and consist of a single ferroelectric domain. The electric polarization can be switched by an electric field applied along the cubic direction, and only 71° rotation of \mathbf{P} is observed. Magnetic state in BFO is chiral and for a given wave vector the spiral is of a single helicity defined by the symmetry of the system via the direction of \mathbf{P} . The equivalent spiral domains can be reversibly controlled by an electric field, and a chiral magnetic state with a single- τ spiral can be stabilized by a field-induced strain in the entire crystal. This is a highly unusual way of achieving chiral resolution and of controlling the magnetic state. These properties of single-crystal BFO make it a promising system for multiferroics research and experimental device fabrication.

This work was supported by the NSF under Grants No. DMR-0704487 and No. DMR-0520471.

¹S.-W. Cheong and M. Mostovoy, *Nat. Mater.* **6**, 13 (2007).

²T. Zhao, A. Scholl, F. Zavaliche, K. Lee, M. Barry, A. Doran, M. P. Cruz, Y. H. Chu, C. Ederer, N. A. Spaldin, R. R. Das, D. M. Kim, S. H. Baek, C. B. Eom, and R. Ramesh, *Nat. Mater.* **5**, 823 (2006).

³W. Eerenstein, N. D. Mathur, and J. F. Scott, *Nature (London)* **442**, 759 (2006).

⁴R. Ramesh and N. A. Spaldin, *Nat. Mater.* **6**, 21 (2007).

⁵Y.-H. Chu, L. W. Martin, M. B. Holcomb, M. Gajek, S.-J. Han, Q. He, N. Balke, C.-H. Yang, D. Lee, W. Hu, Q. Zhan, P.-L. Yang, A. Fraile-Rodriguez, A. Scholl, S. X. Wang, and R. Ramesh, *Nat. Mater.* **7**, 478 (2008).

⁶B. Van Aken, J.-P. Rivera, H. Schmid, and M. Fiebig, *Nature (London)* **449**, 702 (2007).

⁷S. Lee, W. Ratcliff II, S.-W. Cheong, and V. Kiryukhin, *Appl. Phys. Lett.* **92**, 192906 (2008).

⁸D. Lebeugle, D. Colson, A. Forget, M. Viret, A. M. Bataille, and A. Goukasov, *Phys. Rev. Lett.* **100**, 227602 (2008).

⁹I. Sosnowska, T. Peterlin-Neumaier, and E. Stechele, *J. Phys. C*

15, 4835 (1982).

¹⁰J. M. Moreau, C. Michel, R. Gerson, and W. J. James, *J. Phys. Chem. Solids* **32**, 1315 (1971).

¹¹S. K. Streiffer, C. B. Parker, A. E. Romanov, M. J. Lefevre, L. Zhao, J. S. Speck, W. Pompe, C. M. Foster, and G. R. Bai, *J. Appl. Phys.* **83**, 2742 (1998).

¹²R. Przenioslo, M. Regulski, and I. Sosnowska, *J. Phys. Soc. Jpn.* **75**, 084718 (2006).

¹³A. M. Kadomtseva, A. K. Zvezdin, Yu. F. Popov, A. P. Pyatakov, and G. P. Vorob'ev, *JETP Lett.* **79**, 571 (2004).

¹⁴I. Sosnowska and A. K. Zvezdin, *J. Magn. Magn. Mater.* **140-144**, 167 (1995).

¹⁵S. W. Lovesey, *Theory of Neutron Scattering from Condensed Matter* (Oxford University Press, Oxford, 1984).

¹⁶F. Kubel and H. Schmid, *J. Cryst. Growth* **129**, 515 (1993).

¹⁷J. Jacques, A. Collet, and S. H. Wilen, *Enantiomers, Racemates, and Resolutions* (Wiley, New York, 1981).

¹⁸Y. Yamasaki, H. Sagayama, T. Goto, M. Matsuura, K. Hirota, T. Arima, and Y. Tokura, *Phys. Rev. Lett.* **98**, 147204 (2007).